RESEARCH ARTICLE

ADVANCED FUNCTIONAL MATERIALS
www.afm-journal.de

Quasi-Ordered Nanoforests with Hybrid Plasmon Resonances for Broadband Absorption and Photodetection

Mao Li, Meng Shi, Bin Wang, Chenchen Zhang, Shuai Yang, Yudong Yang, Na Zhou, Xin Guo, Dapeng Chen, Shaojuan Li, Haiyang Mao,* and Jijun Xiong**

With the continuing development of green energy technology, solar energy is the most widely distributed and easily utilized form of energy in nature. High-absorption absorbers over a wide spectrum range are beneficial for solar energy harvest. Herein, a fast and efficient method is developed to fabricate a broadband absorber consisting of quasi-ordered nanoforests and metal nanoparticles using a simple plasma bombardment process on a 4-inch silicon wafer, offering high throughputs that can meet practical application demands. The absorber exhibits high absorption exceeding 90% from 300 to 2500 nm, good absorption stability with negligible disturbance from the polarization and the incident angle of light. This effective absorption behavior can be ascribed to multilevel hybridization of the plasmon resonances in the hybrid structures and cavity mode resonances inside the nanoforests. Furthermore, the absorber is integrated onto a thermopile for photodetection with largely enhanced photoresponse from 532 to 2200 nm. The photoinduced voltage of the devices shows a large increment of 433% at 100 mW cm^{-2} light power density, in comparison with a contrast pristine thermopile. It is expected that such a broadband absorber holds great potential for multiple applications, including solar steam generation, photodetection, and solar cells.

1. Introduction

Solar energy has been deemed as a renewable, free, clean, and widely available energy resource. It has attracted widespread attention in recent years to explore materials or structures that have a high absorption coefficient over a broadband spectrum range for utilization of the solar energy. It should be noted that better absorption capability of a broadband absorber could provide higher utilization efficiency of solar energy. To date, different structures and materials that offer high light absorption over a wide range of wavelengths have been explored for optoelectronic and photothermal applications.[1–9] For instance, micro- or nano-structures based on titanium dioxide (TiO_2), silicon (Si), silver (Ag), and aluminum (Al), have been demonstrated with near-blackbody absorption properties in previous studies.[10–17] Among them, black silicon is a typical type of these structures and can achieve visible light absorption of up to ≈90%.[18] Besides, metals are also widely used in these structures because the free carriers in metal films can respond to incident electromagnetic field and form surface plasmon resonances (SPR), enabling high light absorption in a specific wavelength range.[19–29] In the past years, the light absorption feature of metal nanostructures has drawn tremendous research interest due to their advantages in terms of high absorption efficiency and good compatibility with traditional Si-based process technologies.[30–36] The sandwich structures comprising metal nanostructures/dielectric layer/metal plane can achieve near-unity absorption of light at the resonant frequencies.[37,38] Notably, high absorption of these nanostructures only appears at specific frequencies limited by the nature of metal plasmonic resonances. To extend the absorption wavelength range, metal nanoparticles with random dimensions have been fabricated onto a dielectric layer and exhibited multiple absorption peaks that were ascribed to the plasmonic resonances of the nanoparticles with various sizes.[39] High absorption was thus achieved over a broader wavelength range,

---

M. Li, M. Shi, C. Zhang, S. Yang, Y. Yang, Dr. N. Zhou, Prof. D. Chen,
Prof. H. Mao
Institute of Microelectronics of Chinese Academy of Sciences
Beijing 100029, P. R. China
E-mail: maohaiyang@ime.ac.cn

M. Li, Dr. B. Wang, Dr. N. Zhou, Prof. D. Chen, Prof. S. Li, Prof. H. Mao
University of Chinese Academy of Sciences (UCAS)
Beijing 100049, P. R. China

Dr. B. Wang, Prof. S. Li
State Key Laboratory of Applied Optics
Changchun Institute of Optics Fine Mechanics and Physics
Chinese Academy of Sciences
Changchun 130033, P. R. China
E-mail: lishaojuan@ciomp.ac.cn

C. Zhang, S. Yang, Dr. X. Guo, Prof. J. Xiong
National Key Laboratory for Electronic Measurement Technology
North University of China
Taiyuan 030051, P. R. China
E-mail: xiongjijun@nuc.edu.cn

Prof. D. Chen, Prof. H. Mao
Wuxi Internet of Things Innovation Center Co., Ltd.
Wuxi 214001, P. R. China

The ORCID identification number(s) for the author(s) of this article can be found under https://doi.org/10.1002/adfm.202102840.

DOI: 10.1002/adfm.202102840

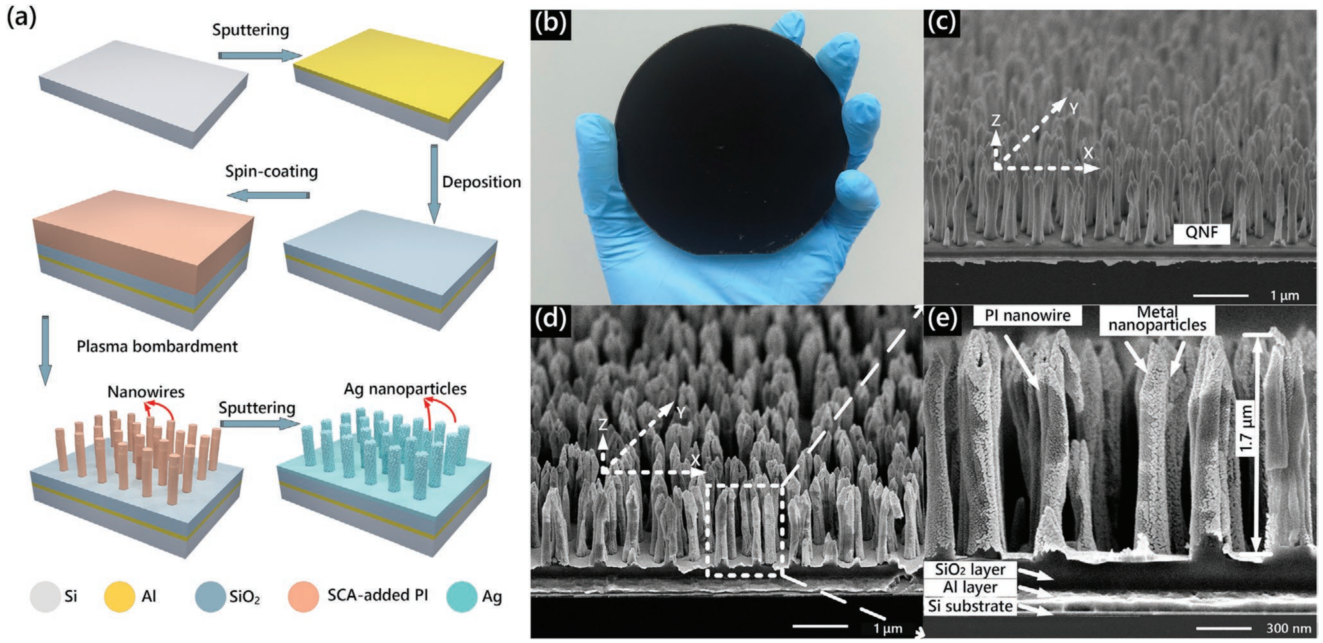

Figure 1. a) Fabrication process of the broadband Ag-QNF absorber using a plasma bombardment on SCA-added PI approach. b) An optical image of the fabricated Ag-QNF absorber on a 4-inch silicon wafer. c–e) SEM images of the QNF and the fabricated Ag-QNF absorber.

but was still limited and generally remained within the visible or near-infrared (NIR) ranges.[40–43] In addition, the absorption properties of such a relatively perfect absorbing structure are usually affected by the incident angle and the polarization state of the light, which causes waste of solar energy.[44–48]

In addition, the fabrication of the current broadband absorbers often requires high-end technologies such as electron beam lithography, focused ion beam etching, or femtosecond laser-assisted etching. Although these technologies can achieve delicate control of the size, morphology, and arrangement at nanometer scale of the nanostructures, most of these methods show low yield and high manufacturing cost, which severely restricts their batch preparation and practical application.[49–55]

In this work, we developed a fast and efficient method to fabricate a novel broadband absorber using plasma bombardment on silane coupling agent (SCA)-added polyimide (PI). This method is demonstrated to be suitable for high-throughput and large-area fabrication of broadband absorbers. This novel broadband absorber is composed of quasi-ordered nanoforests (QNF) that are wrapped with randomly distributed Ag nanoparticles. An average absorption higher than 90% within the wavelength range from 300 to 2500 nm is achieved in this hybrid structure. Simulation results show that this high absorption is caused by multilevel hybridization of plasmon resonances in the hybrid structure and cavity mode resonances inside the QNF, as well as the light trapping abilities of the QNF. Additionally, this near-blackbody absorption is insensitive to both the polarization and the incident angle of light. Finally, the broadband absorber was integrated onto a thermopile for efficient broadband photodetection. The device demonstrates enhanced photoresponse with a large increment of output voltage which is 433% at 100 mW cm^{-2} light power density, in comparison with that of a contrast pristine thermopile. It is expected that the absorber presented in this work holds a great potential for a wide range of applications where effective light absorption is required, possibly expanding the science and device applications in this area.

2. Results and Discussion

2.1. Preparation of the Absorber

2.1.1. Preparation and Characterization of the Quasi-Ordered Nanoforests and Absorber

The process for preparation of the broadband absorber based on QNF using plasma bombardment on SCA-added PI is illustrated in **Figure 1**a. The process began with physical sputtering of an Al layer and chemical vapor deposition of a SiO_2 layer on a 4-inch Si wafer. The layer thicknesses of Al and SiO_2 were 150 and 450 nm, respectively. Meanwhile, PI solution was mixed thoroughly with SCA which occupied 20% content of the mixture, then the SCA-added PI was spin-coated on top of the SiO_2 layer, and the thickness of this layer was controlled to be ≈3.5 µm. Next, a plasma bombardment on SCA-added PI procedure was applied to form nanowire forests, which are defined as the QNF in this work. After that, Ag nanoparticles were sputtered on surfaces of the nanoforests. Consequently, an absorber based on Ag-QNF on an Al–SiO_2 substrate was successfully prepared, which is referred to as Ag-QNF absorber in the following part. Meanwhile, a QNF absorber without Ag nanoparticles located on an Al–SiO_2 substrate (referred to as QNF absorber) and the pristine Al–SiO_2 substrate were also prepared for comparison.

An optical image of the fabricated Ag-QNF absorber on a 4-inch Si wafer is shown in Figure 1b. From the image, we

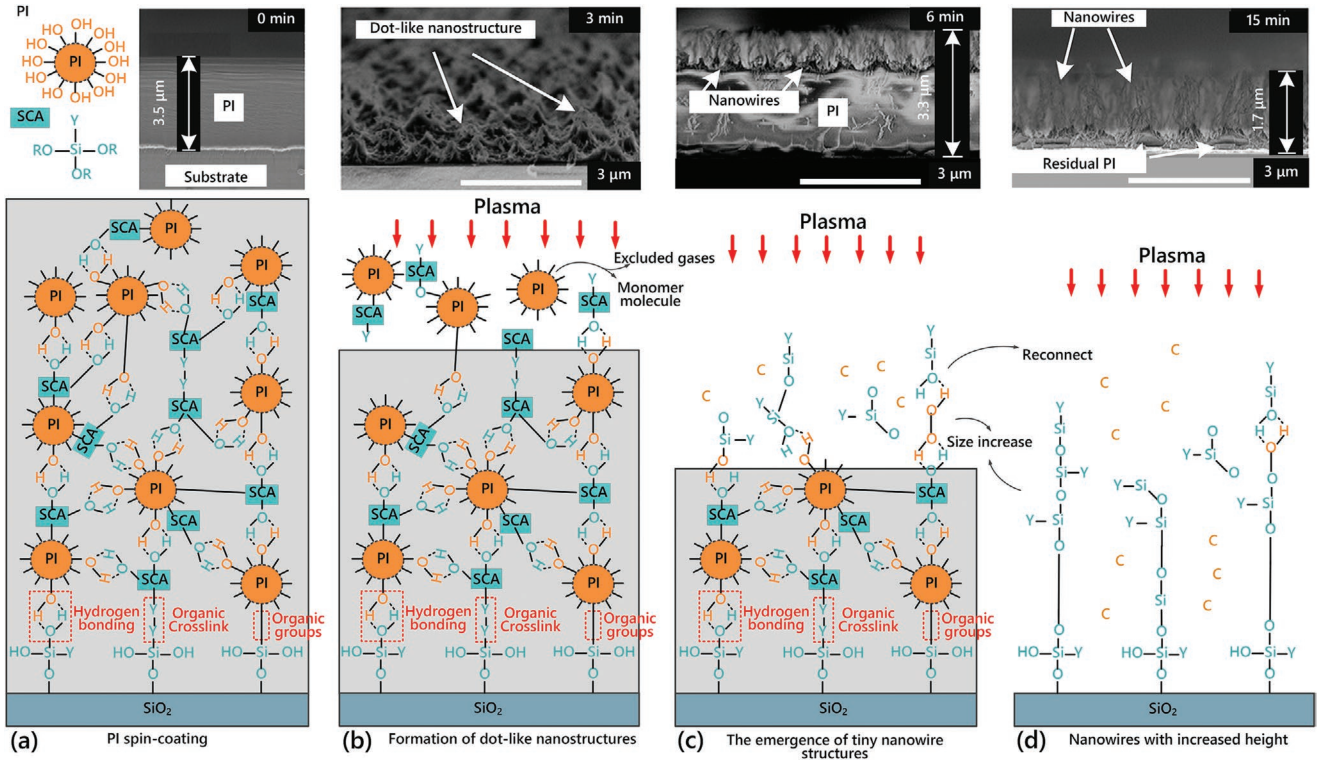

Figure 2. Preparation process and formation mechanism of the QNF using the plasma bombardment on SCA-added PI approach: (a) spin-coating of PI, (b) formation of dot-like nanostructures, (c) the emergence of tiny nanowire structures, and (d) nanowires with increased height.

speculate that it has near-blackbody absorption property. Figure 1c–e shows the scanning electron microscope (SEM) images of the fabricated Ag-QNF absorber. The QNF are composed of many nanowires with a diameter of ≈100 nm, a density of ≈20 μm^{-2}, and a height of ≈1.7 µm. Clearly, nanoscale gaps are formed between the nanowires as shown in Figure 1c. Additionally, Ag nanoparticles with an average diameter of ≈30 nm are distributed randomly on surfaces of the QNF (Figure S1, Supporting Information), while a relatively flat Ag nanofilm is formed at the intervals of the QNF, as seen in Figure 1d,e.

2.1.2. Formation Mechanism of the Quasi-Ordered Nanoforests

The entire process for preparing QNF by plasma bombardment on SCA-added PI is shown in Movie S2, Supporting Information. In the SCA, the organic groups link with each other and hydroxyl groups are bonded to the organic molecules via hydrogen bonding. As shown in Figure S3, Supporting Information, SCA was found to play a unique role in the fabrication process of QNF. The QNF could only be successfully prepared from the PI layers mixed with additional SCA. Moreover, the SCA content also played a crucial role in regulation of nanowire morphology (see Figure S4, Supporting Information).

Figure 2 shows the changes of the sample morphology at the different experimental stages. The formation mechanism of QNF using plasma bombardment on SCA-added PI was explored and summarized as below. As illustrated in Figure 2a, the SCA distributed in the PI layer is in the form of a network (with organic–organic and hydrogen bonding). During the process of the oxygen plasma bombardment, the organic components on surface of the PI layer are decomposed. The organic–organic cross-links on the surface are also broken and the exposed inorganic components of the SCA are left behind. Subsequently, dot-like nanostructures are formed, and this process is accompanied by the production of organic monomer molecules and exhaustible gases, as shown in Figure 2b. With application of further plasma treatment that stimulates and energizes dissociation, the monomer molecular polymers tend to form neutral particles and reaction fragments. The newly generated reaction fragments and inorganic molecules are then combined via hydrogen bonding, where a dehydration condensation reaction also occurs, and a covalent bond is formed to reconnect under the action of plasma bombardment. Therefore, tiny nanostructures in forms of nanowires begin to appear, as shown in Figure 2c. The above process continues under further plasma bombardment, and nanowires with gradually increased heights are formed until the organic components in the PI layer are removed completely, as illustrated in Figure 2d. To further investigate the composition of the fabricated QNF, we prepared QNF on a SiO_2 substrate, and composite structures composed of SiO_2 nanowires and QNF were obtained by using similar etching process as described above. According to the energy-dispersive X-ray (EDX) mapping and the Fourier transform infrared (FTIR) analysis in Figure S5, Supporting Information, the QNF are mainly composed of inorganic substances with Si—O chemical bonds and a small amount of carbon residues. Notably, the composition of the QNF from plasma-treating of SCA-added PI is very close to SiO_2, as seen from Figure S5, Supporting Information.

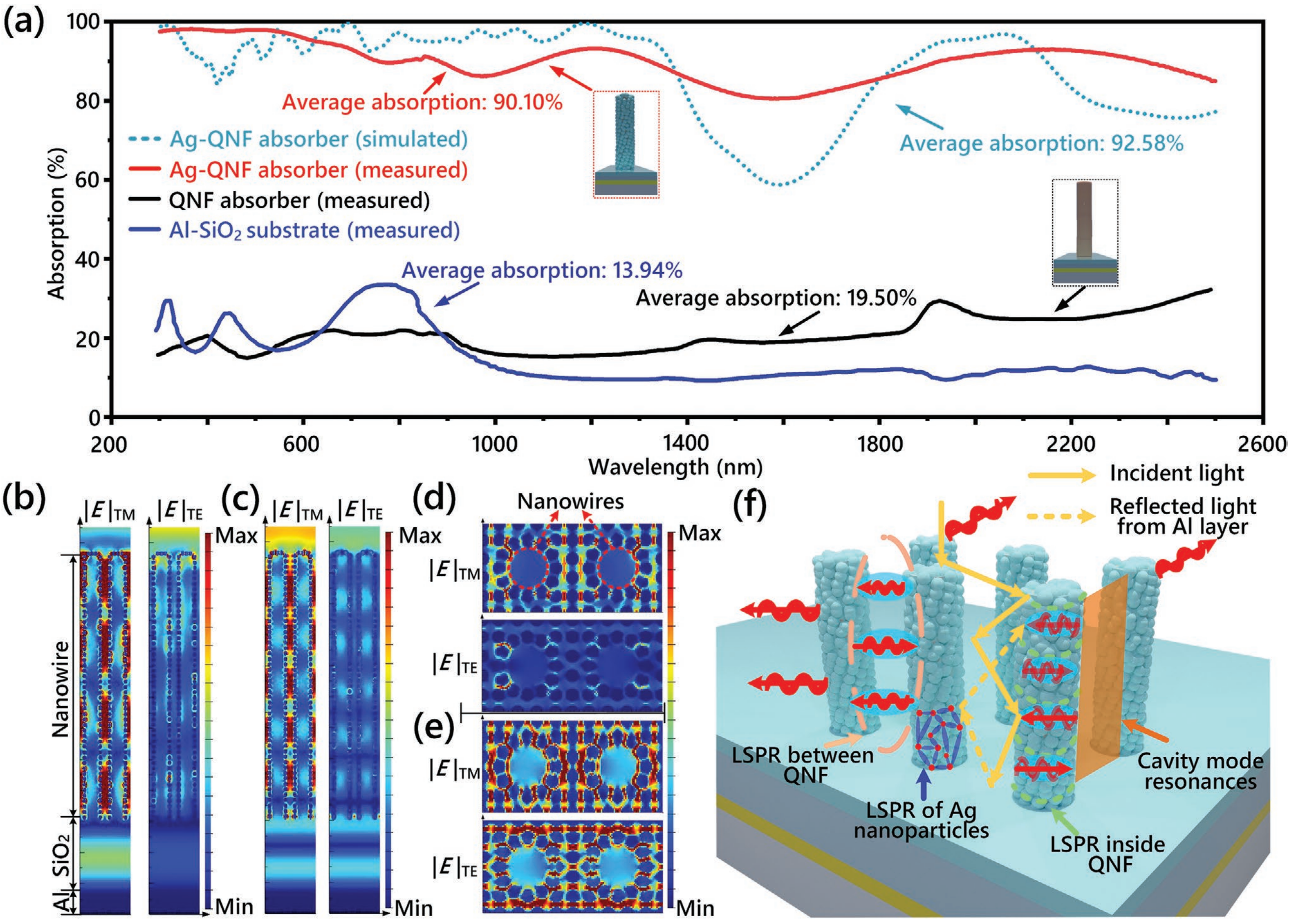

Figure 3. a) Absorption spectra of the Ag-QNF absorber, QNF absorber, and the pristine Al–SiO$_2$ substrate. b,c) Side view of electric field |*E*| distributions at different absorption wavelengths: 1200 nm (b), 850 nm (c). d,e) Top view of electric field |*E*| distributions of Ag nanoparticles on the SiO$_2$ layer at different absorption wavelengths: 1200 nm (d), 850 nm (e). f) Schematic illustration of the light absorption mechanism of the Ag-QNF absorber.

2.2. Optical Characteristics of the Silver-Quasi-Ordered Nanoforests Absorber

2.2.1. Absorption of the Silver-Quasi-Ordered Nanoforests Absorber

Figure 3a shows the absorption spectra of the prepared Ag-QNF absorber, the QNF absorber, and the pristine Al–SiO$_2$ substrate, respectively. The average absorption of the pristine Al–SiO$_2$ substrate is ≈13.94% within the wavelength range from 300 to 2500 nm. While, the absorption of the QNF-absorber is relatively larger (≈19.50%). For the pristine substrate with only the Al and SiO$_2$ layers, the Al layer is used for avoiding transmission, whereas the incident light is reflected almost entirely by the Al layer and only a small portion of the NIR light is absorbed by the SiO$_2$ layer. For the QNF absorber, incident light passing through the QNF to the Al layer is reflected back and reabsorbed or trapped by the QNF, thus leading to a multiple reflection and absorption process and a ≈5.56% enhancement of the average absorption in comparison with pristine Al–SiO$_2$ substrate. Notably, this absorption difference is increased up to more than 10% in the NIR light band.

In stark contrast to the above results, the finally prepared Ag-QNF absorber shows a high absorption of ≈90.10%, as illustrated in Figure 3a. To reveal the mechanism for this broadband high absorption, the electromagnetic field distribution inside the hybrid structure was simulated using the finite difference time domain (FDTD) method, see details in section of Experimental Section. The simulation results are depicted in Figure 3b–e. The electric (*E*) and magnetic (*H*) field distributions inside the absorber were simulated under incident light where the measured absorption spectrum shows obvious peaks (Figure 3a). According to the above analysis in Figure S5, Supporting Information, the composition of the QNF from plasma-treating of SCA-added PI is very close to SiO$_2$, thereby, the value of dielectric constant of QNF was adopted according to the reported value for SiO$_2$.[56] The simulated average absorption of Ag-QNF absorber reaches 92.58%, which is slightly higher than the measured result (≈90.10%). This small discrepancy may be due to the infinitely extended simulation area, which would cause more multiple light reflection and absorption between nanowires.

Figures 3b and d show the side and top views of the distributions of electric field with transverse magnetic (TM) polarization under the incident light of 1200 nm, respectively. The huge enhanced electric field can be observed on both top and side of the nanowires, which means the localized surface plasmon resonance (LSPR) caused by the Ag nanoparticles deposited on the nanowires makes lots of contributions to the high absorption of the absorber.[57,58] Meanwhile, the nanowires which can be regarded as the same function as raster slits show the obvious cavity mode resonances between the nanowires.[59,60] As seen from Figure 3d, the intensity of enhanced electric field stimulated between Ag nanoparticles on the SiO_2 layer is comparable to that between the nanowires, meaning that LSPR of Ag nanoparticles on the SiO_2 layer also plays an important role for the high absorption. For the transverse electric (TE) polarization, the electric field mainly exists on the top and inside the nanowires, indicating a guided mode resonance.[53,61] The electric field distributions under 850 nm incident light is shown in Figure 3c,e, which has similar phenomena as that under 1200 nm. Furthermore, we simulated the distributions of the electric field under the incident light of 2200 nm, as shown in Figure S6, Supporting Information. In general, the above LSPR with different resonant modes all contribute to the high absorption at these wavelengths. With the changes of the geometries of the structure, we also see different resonant modes in the structure (see Figure S7, Supporting Information).

Notably, for the fabricated Ag-QNF absorber, there are discrepancy among the sizes and gaps of the Ag nanoparticles, the gaps between the nanowires, and the homogeneity of the nanowires. All these dimensional differences may cause oscillations of the light absorption at different wavelengths, and the overlap of the peaks at these wavelengths results in a high absorption over a broad wavelength range. In addition to the above LSPR with different resonant modes, reflection of the light by the Al layer and the light-trapping behavior of the QNF also helps to enhance the absorption. Light trapping effect happens because the nanowires have high aspect ratios with an average value of 1.7 µm for height and 100 nm for diameter, and are distributed densely on the substrate. Based on above analysis, the mechanism for the high absorption of the Ag-QNF absorber can be summarized, as is shown in Figure 3f. When light enters into the Ag-QNF structure, most of the light is absorbed because of the LSPR effect of Ag nanoparticles or the light trapping effect. A small portion of the light transmitting through the QNF to the substrate is absorbed by the SiO_2 layer. The residual light reaching the Al layer is reflected back and absorbed again by the Ag-QNF, thereby increasing the overall light absorption of the absorber.

2.2.2. Polarization and Angle Independence of the Silver-Quasi-Ordered Nanoforests Absorber

To investigate the influence of the light polarization on the absorber, the absorption spectra of the Ag-QNF absorber under irradiation of light with different polarizations is plotted in **Figure 4**a,b. It can be seen from Figure 4a that the measured light absorption of the absorber illuminated by TM-polarized light is slightly higher than that when illuminated by TE-polarized light, but this small discrepancy is negligible considering both of their high value reaches ≈90%. As shown in Figure 4a, since the distribution of Ag nanoparticle on the QNF is basically symmetrical in the X–Y plane, this symmetric distribution yields almost the same optical responses for the TM and TE polarizations. Therefore, when incident light with different polarizations stimulates SPR along the X and Y axes, the high light absorption caused by the plasmon resonance behavior is almost independent on the incident polarization of light over the wavelength. To further investigate the influence of different polarization angles on the absorption properties of the absorber, the absorption properties of the absorber was also evaluated using FDTD simulation and the results are shown in Figure 4b. It can be seen from the cloud graphic that the changing trends of the absorption under TM and TE polarization are consistent with the experiment data. Notably, the absorption from 0° to 90° polarization demonstrates similar trend under different incident wavelengths. For all the polarizations, the average absorption of our absorber remains at a value of over 85.05%.

Next, we investigated the influence of incident angle of light on the absorption properties of the absorber. The angle at which the light was incident on the absorber was varied from 0° to 60° with a step of 10°, and the optical reflection and transmission properties of the absorber were then measured at each step, as shown in Figure 4c. It is clearly seen that the average absorption of our absorber remains at a value of larger than 89.34% regardless of the angles. In addition, it should be noted that as the incident angle of light increases, the position of the spectral absorption peak also shifts accordingly. This occurs because the direction of the corresponding electric field is also changed when the angle of incident light changes. Figure 4d depicts the corresponding simulation results of the dependence of absorption properties on the incident angles of light on the absorber. The average absorption value is ≈80.41% at different incident angles of light, and there is no significant reduction as the angle changes from 10° to 60°.

3. Photodetection Applications

To demonstrate application prospects of the structure, the Ag-QNF absorber was integrated onto a thermopile for broadband photodetection. The photoresponse performance of three different types of devices is compared in **Figure 5**. In the figure, the pristine thermopile, the QNF absorber integrated thermopile and the Ag-QNF absorber integrated thermopile are denoted as S1, S2, and S3, respectively. The fabrication process of the devices is detailed in Figure S8, Supporting Information. Figure 5a,b shows the device schematic diagram and optical images. For a typical thermopile device, see Figure 5a, temperature difference between hot and cold ends of thermocouple strips could generate thermal current, and consequently, a photoinduced voltage is generated. For the Ag-QNF absorber integrated thermopile (Figure 5b), the absorption of incident light could be largely enhanced by the Ag-QNF absorber, and strengthened photothermal effect could be stimulated subsequently.[62,63] The photothermal effect-induced thermal energy could pass through the SiO_2 layer to the Al layer, and finally reach the Si_3N_4 layer, where Si_3N_4 acts as an efficient thermal conductive layer. As a result, the hot ends connected to Si_3N_4 of the thermopile were heated up, introducing a temperature difference between the hot and cold ends. Figure 5c compares the photoinduced voltages of the three devices under illumination of different incident light power densities. During

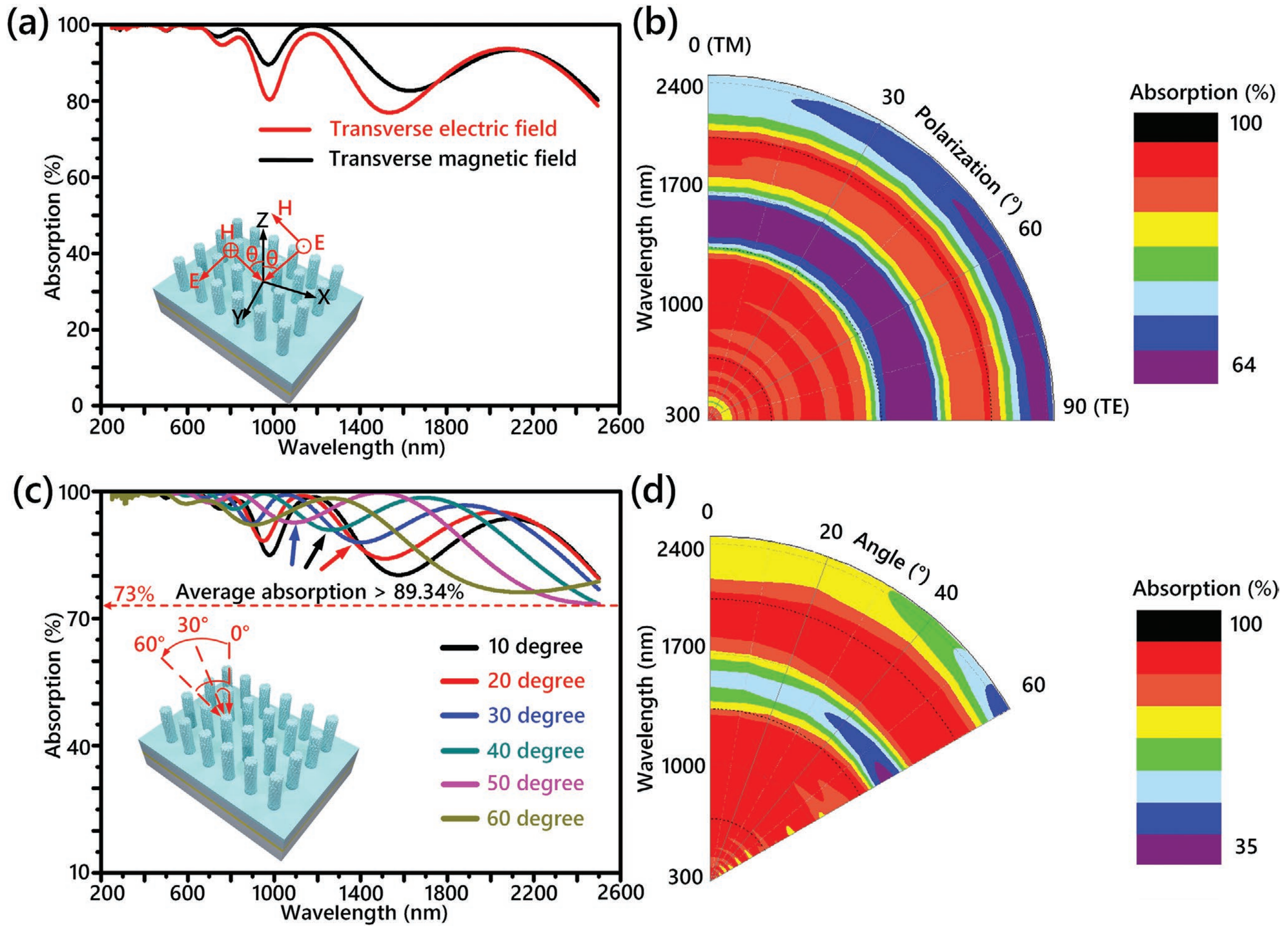

Figure 4. a) Polarization dependence of the absorber over a broadband spectrum. b) Simulated absorption properties under different polarization angles. Here, 0° of polarization angle represents TM polarization, and 90° of polarization angle represents the TE polarization. c) Dependence of absorption properties on the incident angles of light on the absorber. d) Simulated absorption properties under different incident angles of light.

the experiment, a broadband light source equipped with a Xenon lamp capable of controlling light power densities was used to illuminate the devices and the corresponding electrical responses of the devices were measured. The maximum incident light power density used was 100 mW cm^{-2}, which is close to that of the sunlight. As is shown in Figure 5c, the photoinduced voltages of S3 show a dramatic increment of 433% when compared with S1, and an increment of 329% compared with S2, at 100 mW cm^{-2} power density.

Sensitivity of the thermopile can be defined as the ratio of the output voltage change to the light power density change, as expressed in Equation (1)

$$S = \Delta V / \Delta P_{\mathrm{d}} \tag{1}$$

where S represents sensitivity, ΔV represents change of the output voltage, and ΔP_{d} represents change of the light power density. According to Equation (1), sensitivity of the device under illumination reaches 96.5 mV cm^{-2} W^{-1}, obtaining a large enhancement of nearly five times larger than S1 and about thrice larger than S2.

To further demonstrate the broadband photodetection capability, the photoresponse behavior of the devices under different incident light wavelengths from 532 to 2200 nm was investigated, as is shown in Figure 5d. The incident light power was fixed at 40 mW. The output voltage of S3 obtained increments of 377% and 248% when compared with S1 at 808 and 980 nm, respectively, where all these samples show highest and lowest output voltages, as is illustrated in Figure 5d. We have also measured the photoresponse performance of ten thermopile devices integrated with the absorber under the same illumination condition (Figure S9, Supporting Information). The results demonstrate that the performance of the absorber shows good repeatability. In addition, the response time of S3 was also measured and shown in Figure S10, Supporting Information. As is indicated, the device shows a rise time of 14 ms and a fall time of 15 ms, respectively. Overall, the device integrated with the Ag-QNF absorber prepared in this work achieved high-efficiency photothermal and thermoelectric conversion. An application prospect in related fields is highly expected for such a structure.

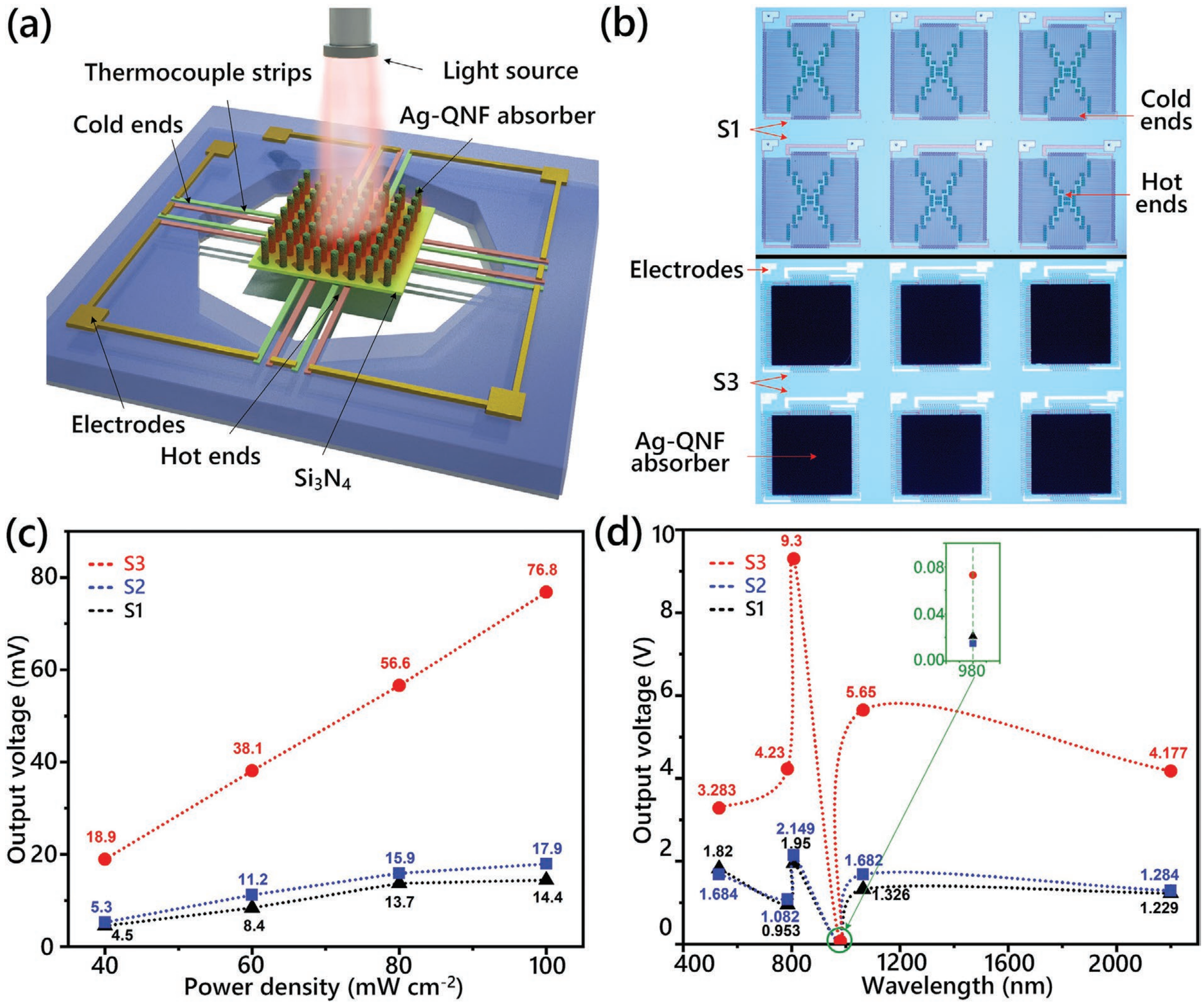

Figure 5. a) Schematic diagram and b) optical images of the pristine thermopiles (S1) and thermopiles integrated with the Ag-QNF absorber (S3). c) Photoinduced voltages of the three devices under different illumination power densities. d) Output voltages of the three devices under different light wavelengths.

4. Conclusion

In conclusion, we presented a high-absorption absorber over a wide range of spectrum based on Ag-QNF using an efficient and simple approach by plasma bombardment on SCA-added PI. The absorption of our absorber reaches 90% over a broadband wavelength range of 300–2500 nm, which can be attributed to the hybrid LSPR effect and the cavity mode resonances in the Ag-QNF, as well as light trapping effect of the QNF. In addition, the absorption of the Ag-QNF absorber is insensitive to the polarization and the incident angle of light. We also integrated the Ag-QNF absorber onto a thermopile for efficient broadband photodetection, and the device demonstrated enhanced photodetection responses from 532 to 2200 nm, with a largest increment of 433% when compared with a pristine thermopile. Such a broadband absorber with hybrid plasmonic effect is expected to be applicable to a diverse range of fields, including optical imaging, photovoltaic devices, solar desalination, and plasmon-enhanced photocatalysis.

5. Experimental Section

Preparation of the Silver-Quasi-Ordered Nanoforests Absorber: In the process for preparation of the QNF, PI (ZKPI-5400) and SCA were used (Bomi Technology, Beijing, China). The two reagents were mixed thoroughly in certain proportions. Then, the reactive ion etching was performed using RIE-100 at Institute of Microelectronics of Chinese Academy of Sciences, Beijing, China. In this step, the applied radio-frequency power was 200 W, the oxygen (O_2) flow rate was 50 sccm, and the Argon (Ar) flow rate was 20 sccm. The treatment periods for O_2 and Ar were 9 and 25 min, respectively. Finally, Ag nanoparticles were sputtered using sputterer (JPFD-400D) at Beiyi Innovation Vacuum Technology, Beijing, China. In this step, the chamber pressure was 5×10^{-4} kPa and the sputtering time was 9 s. And the Ag thickness was controlled to be 30 nm. Consequently, the Ag-QNF absorber was successfully prepared.

Characterization: The morphological features of both the QNF and the corresponding Ag-QNF absorber were acquired using a high-resolution SEM (S-5500, Hitachi, Japan). A transmission electron microscope system (Talos F200X, FEI, USA) equipped with an EDX analysis capability was used to investigate the microstructures and elementary composition of the QNF. FTIR analysis (INVENIO S, BOG, Germany) was used to perform chemical bonds analysis. The absorption property was measured with an UV–vis–NIR spectrophotometer (Cary 7000, Agilent Technologies Inc., USA) equipped with an integrating sphere (150 nm diameter). During the measurement, the wavelength range of the light source was set from 300 to 2500 nm while the spot size of the incident light was 8 mm by 8 mm, and each of the spectra was obtained with an integration time of 2 s.

Physical Modeling: To reveal the physical mechanism of the broadband absorber, the FDTD method was used to simulate the absorption property of the QNF structure. A commercial FDTD package known as Lumerical solutions (Lumerical Inc.) was used to calculate the optical properties and electromagnetic field distributions of the QNF. Perfectly matched layers were used to absorb the scattered radiation in *z*-direction, and periodic boundary conditions were used to perform periodic array in *x*- and *y*-directions. The models were illuminated using a plane wave with TM and TE polarizations from the top of the QNF. An ultrafine mesh size of 5 nm was used in all the simulations. Two monitors were used to calculate the reflection and transmission spectra. Herein, the sizes of nanowires were set at average values according to the SEM measurement results, where the height of the nanowires was 1.7 µm and the diameter of the nanowire was 100 nm with the distance between two nanowires to be ≈100 nm. Ag nanoparticles with 30 nm diameters were arranged densely and discontinuously over the nanowires. Thus, the transmission $T(\lambda)$ and reflection $R(\lambda)$ properties of the structures were simulated, and the relationship between the transmission $T(\lambda)$, reflection $R(\lambda)$, and absorption $A(\lambda)$ could be described using the formula $A(\lambda) = 1 - T(\lambda) - R(\lambda)$, and the absorption $A(\lambda)$ of the structure was calculated from the results of the transmission $T(\lambda)$ and reflection $R(\lambda)$. The electromagnetic fields under both TM and TE polarizations and different incident angles of light were also simulated.

Supporting Information

Supporting Information is available from the Wiley Online Library or from the author.

Acknowledgements

This work was supported by the National Natural Science Foundation of China (Grant No. 61771467, 62022081, and 61974099), Youth Innovation Promotion Association of the Chinese Academy of Sciences (Grant No. 2018153), Special Project for Research and Development in Key areas of Guangdong Province (Grant No. 2019B010117001), Innovation Research Group Project of the National Natural Science Foundation of China (Grant No. 51821003), and National Key Research and Development Program of China (No. 2016YFA0201900 and 2016YFA0201902).

Conflict of Interest

The authors declare no conflict of interest.

Data Availability Statement

The data that support the findings of this study are available from the corresponding author upon reasonable request.

Keywords

broadband photodetectors, hybrid plasmon resonances, light trapping, plasma bombardment process, quasi-ordered nanoforests

Received: March 23, 2021
Revised: May 23, 2021

[1] Z. Liu, G. Liu, Z. Huang, X. Liu, G. Fu, *Sol. Energy Mater. Sol. Cells* **2018**, *179*, 346.
[2] B. Liang, H. Huang, Z. Liu, G. Chen, G. Yu, T. Luo, L. Liao, D. Chen, G. Shen, *Nano Res.* **2014**, *7*, 272.
[3] X. Zhao, X. Zha, L. Tang, J. Pu, W. Yang, *Nano Res.* **2020**, *13*, 255.
[4] J. U. Kim, S. J. Kang, S. Lee, J. Ok, Y. Kim, S. H. Roh, H. Hong, J. K. Kim, H. Chae, S. J. Kwon, T. Kim, *Adv. Funct. Mater.* **2020**, *30*, 2003862.
[5] H. A. Atwater, A. Polman, *Nat. Mater.* **2010**, *9*, 205.
[6] M. Zhu, Y. Li, G. Chen, F. Jiang, F. Yang, X. Luo, Y. Wang, S. D. Lacey, J. Dai, C. Wang, C. Jia, J. Wan, Y. Yao, A. Gong, B. Yang, Z. Yu, S. Das, L. Hu, *Adv. Mater.* **2017**, *29*, 1704107.
[7] Z. Huang, H. Chen, Y. Huang, Z. Ge, Y. Zhou, Y. Yang, P. Xiao, J. Liang, T. Zhang, Q. Shi, G. Li, Y. Chen, *Adv. Funct. Mater.* **2017**, *28*, 1704363.
[8] G. Liu, X. Liu, J. Chen, Y. Lin, L. Shi, G. Fu, Z. Liu, *Sol. Energy Mater. Sol. Cells* **2019**, *190*, 20.
[9] J. Zhou, Z. Liu, G. Liu, P. Pan, X. Liu, C. Tang, Z. Liu, J. Wang, *Opt. Express* **2020**, *28*, 36476.
[10] C. Han, Y. Wang, Y. Lei, B. Wang, N. Wu, Q. Shi, Q. Li, *Nano Res.* **2015**, *8*, 1199.
[11] L. Zhou, X. Yu, J. Zhu, *Nano Lett.* **2014**, *14*, 1093.
[12] H. Wisnu, E. Firat, Y. Selcuk, T. Rasit, *Sol. Energy Mater. Sol. Cells* **2018**, *180*, 247.
[13] N. Liu, H. Liu, S. Zhu, H. Giessen, *Nat. Photonics* **2009**, *3*, 157.
[14] J. van de Groep, P. Spinelli, A. Polman, *Nano Lett.* **2012**, *12*, 3138.
[15] Z. Wang, C. Yang, T. Lin, H. Yin, P. Chen, D. Wan, F. Xu, F. Huang, J. Lin, X. Xie, M. Jiang, *Adv. Funct. Mater.* **2013**, *23*, 5444.
[16] H. Ullah, Y. Qu, T. Wang, Y. Wang, Z. Jing, Z. Zhang, *Appl. Surf. Sci.* **2019**, *467*, 684.
[17] N. I. Landy, S. Sajuyigbe, J. J. Mock, *Phys. Rev. Lett.* **2008**, *100*, 207402.
[18] H. Zhong, A. Guo, G. Guo, W. Li, Y. Jiang, *Nanoscale Res. Lett.* **2016**, *11*, 322.
[19] T. Wen, H. Zhang, Y. Chong, W. G. Wamer, J. Yin, X. Wu, *Nano Res.* **2016**, *9*, 1663.
[20] Y. Cui, Y. He, Y. Jin, F. Ding, L. Yang, Y. Ye, S. Zhong, Y. Lin, S. He, *Laser Photonics Rev.* **2014**, *8*, 495.
[21] X. Fan, W. Zheng, D. J. Singh, *Light: Sci. Appl.* **2014**, *3*, e179.
[22] G. Wang, L. Li, W. Fan, R. Wang, S. Zhou, J. T. Lü, L. Gan, T. Zhai, *Adv. Funct. Mater.* **2018**, *28*, 1800339.
[23] A. M. Angulo, C. Noguez, G. Z. Schatz, *J. Phys. Chem. Lett.* **2011**, *2*, 1978.
[24] L. Au, Y. Chen, F. Zhou, P. H. C. Camargo, B. Lim, Z. Y. Li, D. S. Ginger, Y. Xia, *Nano Res.* **2008**, *1*, 441.
[25] H. Wei, H. Xu, *Nanoscale* **2013**, *5*, 10794.
[26] P. Johns, K. Yu, M. S. Devadas, G. V. Hartland, *ACS Nano* **2016**, *10*, 3375.
[27] D. Darvill, A. Centeno, F. Xie, *Phys. Chem. Chem. Phys.* **2013**, *15*, 15709.
[28] K. Yoshioka, Y. Minami, K. I. Shudo, T. D. Dao, T. Nagao, M. Kitajima, *Nano Lett.* **2015**, *15*, 1036.
[29] J. Chen, S. Chen, P. Gu, Z. Yan, C. Tang, Z. Xu, B. Liu, Z. Liu, *Carbon* **2020**, *162*, 187.
[30] G. Baffou, I. Bordacchini, A. Baldi, R. Quidant, *Light: Sci. Appl.* **2020**, *9*, 108.
[31] X. Liu, T. Tyler, T. Starr, A. F. Starr, N. M. Jokerst, W. J. Padilla, *Phys. Rev. Lett.* **2011**, *107*, 045901.
[32] J. B. Chou, Y. X. Yeng, Y. E. Lee, A. Lenert, V. Rinnerbauer, I. Celanovic, M. Soljačić, N. X. Fang, E. N. Wang, S. G. Kim, *Adv. Mater.* **2014**, *26*, 8041.
[33] A. Moreau, C. Ciracì, J. J. Mock, R. T. Hill, Q. Wang, B. J. Wiley, A. Chilkoti, D. R. Smith, *Nature* **2012**, *492*, 86.
[34] M. Elbahri, M. K. Hedayati, V. S. K. Chakravadhanula, M. Jamali, T. Strunkus, V. Zaporojtchenko, F. Faupel, *Adv. Mater.* **2011**, *23*, 1993.

[35] K. Aydin, V. E. Ferry, R. M. Briggs, H. A. Atwater, *Nat. Commun.* **2011**, *2*, 517.
[36] I. H. Lee, D. Yoo, P. Avouris, T. Low, S. H. Oh, *Nat. Nanotechnol.* **2019**, *14*, 313.
[37] N. Liu, M. Mesch, T. Weiss, M. Hentschel, H. Giessen, *Nano Lett.* **2010**, *10*, 2342.
[38] D. M. Nguyen, D. Lee, J. Rho, *Sci. Rep.* **2017**, *7*, 2611.
[39] G. Liu, Y. Liu, X. Liu, J. Chen, G. Fu, Z. Liu, *Sol. Energy Mater. Sol. Cells* **2018**, *186*, 142.
[40] M. Liu, M. Leng, C. Yu, X. Wang, C. Wang, *Nano Res.* **2010**, *3*, 843.
[41] S. A. Jalil, B. Lai, M. ElKabbash, J. Zhang, E. M. Garcell, S. Singh, C. Guo, *Light: Sci. Appl.* **2020**, *9*, 14.
[42] Z. Liu, X. Liu, S. Huang, P. Pan, J. Chen, G. Liu, G. Gu, *ACS Appl. Mater. Interfaces* **2015**, *7*, 4962.
[43] J. Chen, H. Nie, C. Peng, S. Qi, C. Tang, Y. Zhang, L. Wang, G.-S. Park, *J. Lightwave Technol.* **2018**, *36*, 3481.
[44] Y. Jin, J. Park, Y. Rah, J. Shim, K. Yu, *Sci. Rep.* **2019**, *9*, 9866.
[45] X. Zou, G. Zheng, J. Cong, L. Xu, Y. Chen, M. Lai, *Opt. Lett.* **2018**, *43*, 46.
[46] D. Lee, S. Y. Han, Y. Jeong, D. M. Nguyen, G. Yoon, J. Mun, J. Chae, J. H. Lee, J. G. Ok, G. Y. Jung, H. J. Park, K. Kim, J. Rho, *Sci. Rep.* **2018**, *8*, 12393.
[47] X. Tian, Z. Y. Li, *Photonics Res.* **2016**, *4*, 146.
[48] H. A. Atwater, A. Polman, *Nat. Mater.* **2010**, *9*, 205.
[49] Z. Yang, X. Ding, J. Jiang, *Nano Res.* **2016**, *9*, 787.
[50] I. Pastoriza-Santos, C. Kinnear, J. Pérez-Juste, P. Mulvaney, L. M. Liz-Marzán, *Nat. Rev. Mater.* **2018**, *3*, 375.
[51] J. Geldmeier, T. König, M. A. Mahmoud, M. A. El-Sayed, V. V. Tsukruk, *Adv. Funct. Mater.* **2014**, *24*, 6797.
[52] A. W. Clark, J. M. Cooper, *Adv. Mater.* **2010**, *22*, 4025.
[53] Y. Li, Z. Liu, H. Zhang, P. Tang, B. Wu, G. Liu, *Opt. Express* **2019**, *27*, 11809.
[54] L. Zhou, S. Zhuang, C. He, Y. Tan, Z. Wang, J. Zhu, *Nano Energy* **2016**, *32*, 195.
[55] Z. Liu, H. Zhong, G. Liu, X. Liu, Y. Wang, J. Wang, *Opt. Express* **2020**, *28*, 31763.
[56] E. D. Palik, *Handbook of Optical Constants of Solids*, Academic Press, San Diego, CA **1998**.
[57] P. Yu, H. Yang, X. Chen, Z. Yi, W. Yao, J. Chen, Y. Yi, P. Wu, *Renewable Energy* **2020**, *158*, 227.
[58] J. Li, Z. Chen, H. Yang, Z. Yi, X. Chen, W. Yao, T. Duan, P. Wu, G. Li, Y. Yi, *Nanomaterials* **2020**, *10*, 257.
[59] L. Lei, S. Li, H. Huang, K. Tao, P. Xu, *Opt. Express* **2018**, *26*, 5686.
[60] D. Chanda, K. Shigeta, T. Truong, E. Lui, A. Mihi, M. Schulmerich, P. V. Braun, R. Bhargava, J. A. Rogers, *Nat. Commun.* **2011**, *2*, 479.
[61] R. Feng, J. Qiu, Y. Cao, L. Liu, W. Ding, L. Chen, *Opt. Express* **2015**, *23*, 21023.
[62] A. R. Miandashti, L. K. Khorashad, M. E. Kordesch, A. O. Govorov, H. H. Richardson, *ACS Nano* **2020**, *14*, 4188.
[63] Y. Pan, G. Tagliabue, H. Eghlidi, C. Höller, S. Dröscher, G. Hong, D. Poulikakos, *Sci. Rep.* **2016**, *6*, 37564.